analytica

MDPI

Article

Laser-Induced Fabrication of Binder-Free Hierarchical Ru-Ir Bimetallic Microstructures for Sensitive Dual-Range Non-Enzymatic Glucose Detection

Alexander V. Vavilov [1,2,*], Aleksei P. Zakharov [1], Evgeniia M. Khairullina [3,*], Aleksandra S. Levshakova [1,4], Maria Kaneva [1,4], Stanislav Gurbatov [3,5], Dmitrii M. Nikolaev [1,6], Mikhail N. Ryazantsev [1] and Maxim S. Panov [1,2,6]

1 Institute of Chemistry, Saint Petersburg State University, 7/9 Universitetskaya Emb., Saint Petersburg 199034, Russia; alexzaharov2000forever@gmail.com (A.P.Z.); sashkeens@gmail.com (A.S.L.); skt94@bk.ru (M.K.); dmitrii.m.nikolaev@gmail.com (D.M.N.); m.ryazantsev@spbu.ru (M.N.R.); m.s.panov@spbu.ru (M.S.P.)
2 Nanotechnology Research and Education Centre RAS, Saint Petersburg Academic University, 8/3 Khlopina St., Saint Petersburg 194021, Russia
3 Institute of Automation and Control Processes, Far Eastern Branch, Russian Academy of Sciences, 5 Radio St., Vladivostok 690041, Russia; gurbatov_slava@mail.ru
4 Ioffe Institute, 26 Politekhnicheskaya St., Saint Petersburg 194021, Russia
5 Polytechnic Institute, Far Eastern Federal University, 8 Sukhanova St., Vladivostok 690090, Russia
6 Center for Physical Sciences and Information Technologies, St. Petersburg State Chemical Pharmaceutical University, 14 Professor Popov St., Lit. A, Saint Petersburg 197022, Russia
* Correspondence: sanya050199@gmail.com (A.V.V.); evgeniia.khairullina@gmail.com (E.M.K.)

Abstract

Developing efficient, non-enzymatic glucose sensors is crucial for overcoming the stability and environmental limitations of conventional enzymatic devices. In this work, a series of ruthenium-based bimetallic microstructures (Ru–Ir, Ru–Pt, Ru–Au DMF, and Ru–Au NPs) were successfully fabricated on glass substrates using a mask-free, two-stage laser-induced chemical liquid-phase deposition (LCLD) technique. Among the prepared materials, the binder-free Ru–Ir electrode exhibited the highest electrocatalytic activity toward glucose oxidation in an alkaline medium. Characterization by SEM, EDX, and XRD revealed a highly developed hierarchical surface morphology with distinct metallic phases. Chronoamperometric measurements performed at an operating potential of 0.45 V (vs. Ag/AgCl) demonstrated that the Ru–Ir sensor possesses a dual-range linear calibration—0.5–3000 μM and 3000–12,500 μM—with sensitivities of 0.027 and 0.014 μA μM^{-1} cm^{-2}, respectively. The limit of detection was determined to be 58.1 nM. This improved performance and dual-range linearity are highly likely attributed to the abundance of electroactive sites provided by the hierarchical architecture and a synergetic effect between Ru and Ir that accelerates surface-controlled glucose dehydrogenation. Furthermore, the Ru–Ir sensor demonstrated negligible cross-sensitivity toward common interferents, an electrode-to-electrode RSD of 2.33% (n = 5), and remarkable long-term stability, retaining over 85% of its initial response after 30 days. Overall, the two-stage LCLD procedure provides a mask-free, binder-free, and direct-write route for fabricating bimetallic electrodes under ambient conditions.

Keywords: non-enzymatic electrochemical glucose sensor; laser-induced chemical liquid-phase deposition (LCLD); bimetallic microstructures; ruthenium; iridium; gold; platinum; hierarchical structures

Academic Editor: Arnaldo César Pereira

Received: 3 August 2026
Revised: 5 September 2026
Accepted: 10 September 2026
Published: 12 September 2026

1. Introduction

Diabetes is a chronic metabolic disorder characterized by high blood glucose levels. In diabetes, the body either cannot produce insulin—a hormone that helps regulate blood glucose levels—or cannot effectively use the insulin it produces [1]. Abnormal blood glucose levels can cause various health complications, such as retinopathy, delayed wound healing, kidney disease, neurological disorders, and cardiovascular diseases [2]. Therefore, it is vital to develop fast, simple, and reliable glucose detection techniques. Several techniques have been developed for glucose detection, including colorimetric analysis [3,4], mass spectrometry [5], fluorescence [6,7], chemiluminescence [8,9], and microfluidic sensors [10]. Despite their advantages, these techniques possess certain drawbacks. For instance, they may involve complex processes, exhibit low reproducibility, suffer from matrix interference, be expensive, and have a limited shelf life [11]. Hence, there is a need to develop more efficient techniques for glucose detection. Electrochemical methods are considered to be the most effective for detecting low concentrations of numerous disease markers, including glucose, because they offer good accuracy, good specificity, good response times, simplicity, lower detection limits, high physical and chemical stability, an enhanced electron transfer rate, practical detectability, and biocompatibility [11]. Electrochemical methods can employ either enzymatic or non-enzymatic sensors [12]. Enzymatic sensors, particularly those utilizing glucose oxidase (GO_x), are currently the most widely used [12]. They exhibit high sensitivity and selectivity [13]; however, they can only be used within a limited range of pH, temperature, and humidity. Furthermore, enzyme immobilization processes are quite complicated, and enzymatic sensors have a short shelf life due to enzyme degradation [14]. In contrast, non-enzymatic sensors lack these drawbacks since the electrocatalytic oxidation of the analyte occurs directly on the electrode surface [15].

Numerous materials have been explored for non-enzymatic electrochemical glucose detection, but many suffer from costly precursors, limited linear ranges, poor detection limits, and low selectivity. Nanostructured metals with highly developed surfaces are therefore promising sensor materials, particularly noble-metal bimetallic structures, which can provide higher catalytic activity, stability, poisoning resistance, synergistic effects, and selectivity than monometallic counterparts [2,16]. Ruthenium is especially attractive as a synergistic promoter in multicomponent systems rather than as a standalone catalyst. In Pt-based systems, Ru can act as an anti-poisoning component through a bifunctional mechanism involving low-potential OH_{ads} species that remove adsorbed CO, whereas in Au-based systems it can enhance glucose chemisorption through ligand and electronic effects. Iridium is also promising for enzyme-free sensing because of its resistance to chloride poisoning, a major limitation of Pt and Au in biological media. In addition, reversible Ir^{3+}/Ir^{4+} redox transitions within IrO_2 can lower the reaction overpotential and increase the density of electroactive surface sites, thereby improving selectivity, stability, and sensitivity [17].

Various techniques are used to fabricate bimetallic structures, including direct laser writing [18], chemical vapor deposition [19], inkjet printing [20], laser ablation [21], and laser sintering [22]. However, these methods suffer from significant drawbacks, such as high equipment costs, the requirement for multi-step surface pre-treatment, and low processing throughput. Furthermore, vacuum-based or high-temperature steps often limit their applicability to temperature-sensitive substrates. To overcome these challenges, laser-induced chemical liquid-phase deposition (LCLD) has emerged as a compelling alternative [23,24], enabling localized, mask-free, direct-write metallization under ambient conditions. Depending on the target architecture, a single LCLD deposition stage can be used for monometallic structures or multimetallic structures obtained by co-deposition, whereas sequentially modified multimetallic architectures require multiple deposition

stages. This technique utilizes a laser to initiate a reduction reaction within a localized volume of a solution. The reaction occurs at the focus of the laser beam, resulting in metal deposition onto the surface of a dielectric substrate. This approach enables the deposition of metal structures of specific sizes onto various types of dielectrics and semiconductors. Due to its ability to produce conductive, porous, nano-sized metal microstructures that exhibit high electrocatalytic activity on almost any surface, this technique is particularly suitable for designing and manufacturing sensor-active materials [25,26]. Previous LCLD-based studies demonstrated sequentially fabricated Ru–Au and Au–Ru architectures for non-enzymatic epinephrine sensing [27,28], as well as Ir-based microstructures successively modified with Au and Pt for glucose detection [29]. The present work advances this platform through a Ru–Ir deposition sequence yielding a hierarchical bimetallic architecture with closely associated Ru- and Ir-containing regions. Relative to the previously reported multimetallic LCLD glucose electrode, the Ru–Ir system extends the calibration range, lowers the calculated detection limit, and provides a longer-term stability assessment. Specifically, the Ru–Ir electrode exhibits two calibration ranges of 0.5–3000 and 3000–12,500 μM, a calculated LOD of 0.0581 μM, and more than 85% response retention after 30 days. These results further demonstrate the versatility of LCLD for tailoring multimetallic electrode composition and hierarchical morphology and support the developed Ru–Ir architecture as an effective platform for broad-range non-enzymatic glucose detection.

2. Materials and Methods

2.1. Laser-Assisted Synthesis of Ruthenium-Based Composites

All noble metal complexes (analytical grade) were obtained from Sigma-Aldrich (St. Louis, MO, USA), and N,N-dimethylformamide (DMF, 99.90%) was purchased from NevaReaktiv (St. Petersburg, Russia). All reagents were used as received. The compositions of the solutions used to fabricate the electrode materials based on ruthenium and other noble metals are presented in Table 1. DMF was used as the solvent to dissolve all metal complexes. Apart from the complex solutions, a solution containing gold nanoparticles was utilized to prepare Ru–Au composites. Hereinafter, the composites obtained using the solution containing Au nanoparticles will be referred to as "Ru–Au NPs" (similar material was fabricated in our previous work [23]), while those obtained using the Au complex solution in DMF will be designated as "Ru–Au DMF".

Table 1. Composition of solutions used for the laser-assisted deposition of ruthenium-based microstructures. In each case, N,N-dimethylformamide was used as the solvent.

Metal	Reagent	Concentration, mM
Ru	triruthenium dodecacarbonyl $Ru_3(CO)_{12}$	5
Ir	tris(2-phenylpyridine) iridium (III), $C_{33}H_{24}IrN_3$	3
Pt	Dichloro(dicyclopentadienyl)platinum(II), $C_{10}H_{12}Cl_2Pt$	6
Au	chloro(triphenylphosphine)gold(I) $[(C_6H_5)_3P]AuCl$	3

The solution containing gold nanoparticles was prepared according to Borovskaya's technique, as described in [27]. Deionized water (95 mL) was poured into a clean conical flask, and 30 μL of a 30% chloroauric acid ($HAuCl_4$) solution was added and heated to 95 °C. Then, 5 mL of a 1% sodium citrate solution was added to the hot $HAuCl_4$ solution, and the mixture was heated almost to boiling. Following the addition of sodium citrate, a blue color appeared, which transitioned to red within a few minutes.

These materials were synthesized using the LCLD technique. A schematic diagram of the experimental setup is shown in Figure 1.

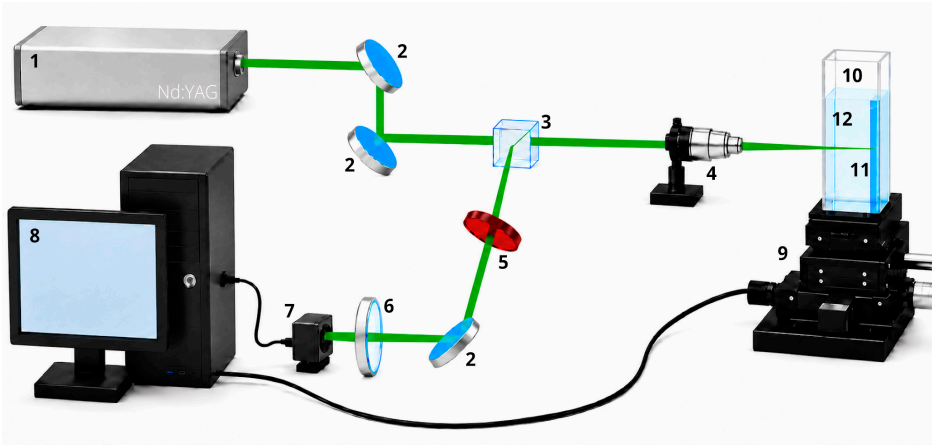

Figure 1. Schematic of the experimental setup for LCLD. (1) Continuous-wave solid-state Nd:YAG laser (λ = 532 nm), (2) mirrors, (3) beam splitter cube, (4) microscope objective, (5) attenuating filter, (6) lens, (7) webcam, (8) computer, (9) translation stage, (10) experimental cell with solution, (11) glass substrate, (12) solution.

The laser beam from a continuous-wave diode-pumped solid-state Nd:YAG laser (λ = 532 nm; Changchun, China) (1) was directed into a beam splitter cube (3) via two aluminum mirrors (2). The laser radiation was then focused using a microscope objective (4) onto the inner surface of the front glass substrate (11) of the experimental cell (10). The cell was mounted on a 3D motorized translation stage (9) controlled by a computer (8). Part of the laser radiation reflected from the cell was directed back through the beam splitter cube, passing through an attenuating filter (5) and a lens (6) into a webcam (7) for real-time process monitoring.

In this study, a two-stage LCLD process was utilized to synthesize Ru–Ir, Ru–Pt, Ru–Au DMF, and Ru–Au NP composites under 532-nm laser irradiation. In the first stage, ruthenium microstructures were deposited onto the glass surface to fabricate a Ru electrode (~10 mm long and ~1 mm wide). In the second stage, iridium, gold, or platinum was deposited onto the surface of the pre-fabricated ruthenium electrode. For both stages, the scanning speed was maintained at 3.75 μm s^{-1} and the laser power was set to 1.4 W. It is worth noting that during the deposition of pre-synthesized gold nanoparticles to form the Ru–Au NP composite, no laser-induced chemical reduction occurred in the experimental cell; instead, laser-driven physical deposition or sintering took place.

2.2. Morphology and Composition Analysis

Scanning electron microscopy (SEM) and energy-dispersive X-ray (EDX) spectroscopy were performed using a Zeiss Merlin scanning electron microscope (Oberkochen, Germany) equipped with an INCA X-Act analyzer (Oxford Instruments, Abingdon, UK). Particle sizes were measured in ImageJ (version 1.54f; National Institutes of Health, Bethesda, MD, USA) for ≥200 particles from ≥3 independent regions per sample. Transmission electron microscopy (TEM) was conducted using a Zeiss Libra 200FE microscope (Oberkochen, Germany).

X-ray diffraction (XRD) patterns of the composites were recorded on a Bruker D2 Phaser diffractometer equipped with a LynxEye detector (Karlsruhe, Germany).

X-ray photoelectron spectra (XPS) were acquired using an Escalab 250Xi spectrometer (Thermo Fisher Scientific, East Grinstead, West Sussex, UK).

2.3. Electrochemical Studies

Electrochemical measurements were performed at 23 ± 2 °C using a Corrtest CS300 potentiostat (Wuhan Corrtest Instruments Co., Ltd., Wuhan, China) in a three-electrode cell initially containing 50.0 mL of 0.1 M NaOH. The fabricated Ru–Ir structure was used as the working electrode, an Ag/AgCl electrode filled with 3.0 M KCl as the reference electrode, and a Pt wire as the counter electrode. The exposed working-electrode dimensions were 1.0 × 10.0 mm, corresponding to a projected geometric area of 0.1 cm^2. Current density was calculated as $j = I/A_{geo}$ without correction for surface roughness. CV measurements were conducted from −0.10 to +0.80 V vs. Ag/AgCl at 50 mV s^{-1}. Five consecutive cycles were recorded, and the third stabilized cycle is presented. No mechanical or chemical pretreatment was applied. Chronoamperometry was performed continuously at +0.45 V after a 900-s baseline-stabilization period. The electrolyte was stirred continuously at 140 rpm, and glucose additions were made at 100-s intervals. The response assigned to each concentration was the mean current density during the final 20 s before the subsequent addition. A 0.100 M glucose stock solution was prepared in 0.1 M NaOH, and lower-concentration working solutions were obtained by volumetric dilution with the same electrolyte. Three independent calibrations were performed using separately fabricated Ru–Ir electrodes and freshly prepared electrolyte and glucose solutions (n = 3). The corresponding calibration data are presented in Table S1. Within each complete calibration experiment, the same Ru–Ir electrode was used continuously for all successive glucose additions across the entire investigated concentration range, including both fitted calibration regions. The selectivity of glucose sensing was evaluated in the presence of common interfering analytes, including dopamine (DA), fructose (Fru), hydrogen peroxide (H_2O_2), ascorbic acid (AA), uric acid (UA), and acetaminophen (AP).

3. Results and Discussion

The composites were synthesized via a two-stage LCLD approach. Initially, ruthenium microstructures were fabricated on the glass substrate, followed by the subsequent deposition of gold, iridium, or platinum. The specific experimental parameters, including the solutions' compositions and the laser irradiation conditions (3.75 μm s^{-1} scanning speed, 532 nm laser wavelength, and 1.4 W laser power), are detailed in Section 2. Based on the optical and photochemical properties of the precursor complexes [28,29], the laser deposition process is thermally induced (pyrolytic), whereas any contribution from photochemical pathways can be disregarded. This thermal mechanism also applies to the deposition of pre-synthesized gold nanoparticles, where laser-induced local heating drives their immobilization.

Scanning electron microscopy, energy-dispersive X-ray spectroscopy, X-ray diffraction, and transmission electron microscopy were employed to characterize the surface morphology and elemental/structural composition of the deposited microstructures (Figures 2–4).

As shown in Figure 2a, the Ru–Pt composite exhibits a Pt layer covering the Ru surface rather than forming individual spherical nanoparticles, which limits any significant increase in the specific surface area. The Ru–Ir composite (Figure 2b) displays a complex hierarchical architecture consisting of spherical nanoparticles (60–400 nm in diameter (inset in Figure 2b)), their agglomerates, and micron-sized pores that also contain nanoparticles. The Ru–Au DMF composite (Figure 2c) features a highly developed hierarchical surface where larger nanoparticles are decorated by smaller ones (20–80 nm). In contrast, the Ru–Au NP composite (Figure 2d) consists of small spherical nanoparticles (~10 nm) and cracks (~0.5 μm wide) that likewise contain nanoparticles. At a larger scale, the SEM image (Figure 2e) corroborates this highly developed surface texture of the Ru–Ir composite, while the corresponding EDS mapping (Figure 2f,g) verifies its elemental composition, revealing

a uniform distribution of Ru and Ir across the catalytic layer. The EDX spectra (Figure 3a) of all ruthenium-based composites confirm the presence of Pt, Ir, or Au alongside Ru; the remaining elements (C, Si, O, Mg, Na, Ca, Cl, Zn, N) originate from the underlying glass substrate and residual solvent. The XRD reflections were assigned using ICDD patterns for hcp Ru (00-006-0663), fcc Ir (00-006-0598), fcc Pt (00-004-0802), and fcc Au (00-004-0784), with characteristic peaks at 38.4, 42.2, 44.0, 58.3, 69.4, and 78.4° (Ru); 40.7, 47.3, 69.2, 83.4, and 88.1° (Ir); 39.8, 46.2, 67.5, 81.3, and 85.7° (Pt); and 38.2, 44.4, 64.6, 77.6, 81.7, and 98.1° (Au). The XRD patterns (Figure 3b) reveal two distinct metallic phases (Ru and the corresponding noble metal) in all samples, with no oxide phases detected within the detection capability of XRD. However, thin, amorphous, poorly crystalline, or low-abundance surface oxides cannot be excluded.

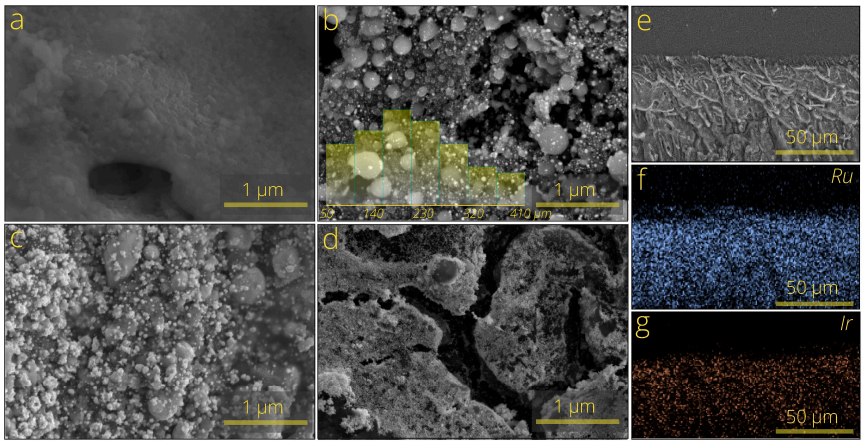

Figure 2. SEM images of the Ru-based composites at different magnifications (**a**–**d**) and of the Ru–Ir electrode (**e**), with corresponding EDS elemental maps of Ru (**f**) and Ir (**g**). The inset in (**b**) shows the particle size distribution histogram for the Ru–Ir composite.

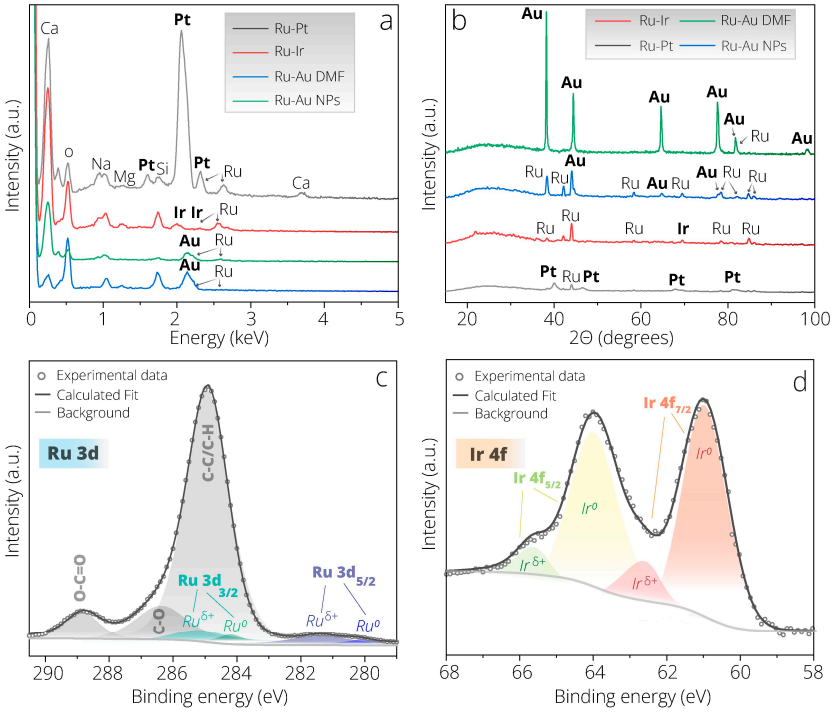

Figure 3. (**a**) EDX spectra and (**b**) XRD patterns of the fabricated Ru-based microstructures; (**c**,**d**) XPS spectra of the Ru–Ir sample in the (**c**) Ru 3d and (**d**) Ir 4f core-level regions.

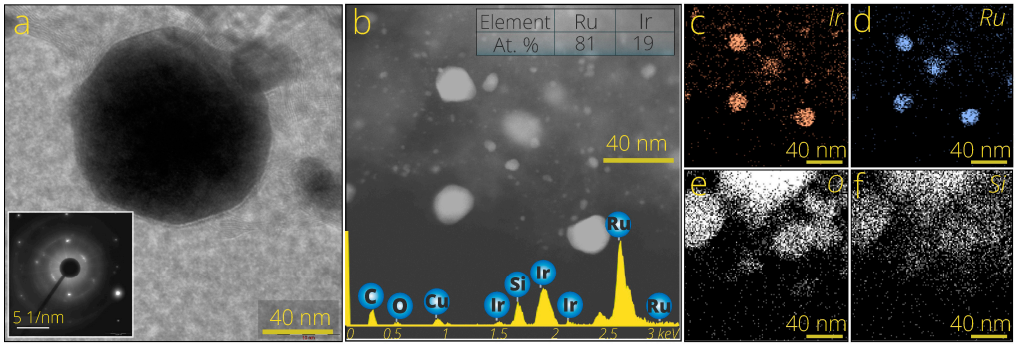

Figure 4. (**a**) HRTEM image of a representative Ru–Ir nanoparticle; the inset shows the corresponding SAED pattern. (**b**) EDX spectrum acquired from the TEM region, and (**c**–**f**) corresponding elemental maps of Ir, Ru, O, and Si, respectively.

XPS results (Figure 3c,d) showed that the Ir 4f (Figure 3d) envelope was best described by a predominant metallic doublet and a minor higher-binding-energy contribution. The Ir^0 $4f_{7}/_{2}$ and $4f_{5}/_{2}$ components were located at 60.87 and 63.87 eV, respectively, and accounted for 80.0% of the fitted Ir 4f doublet area. The remaining contribution, denoted Irδ+, was fitted at 62.50 and 65.50 eV and represented 20.0% of the Ir 4f area. Because oxidized or hydroxylated Ir species can occur in this binding-energy region, no unique Ir oxide stoichiometry was assigned. Joint deconvolution of the Ru 3d and C 1s regions (Figure 3c) resolved a metallic Ru doublet at 280.16 and 284.33 eV together with a higher-binding-energy $Ru^{\delta+}$ doublet at 281.26 and 285.43 eV. The XPS results therefore indicate predominantly metallic Ir and a mixed $Ru^0/Ru^{\delta+}$ surface composition. This surface-sensitive picture is compatible with the metallic reflections observed by XRD: XRD primarily probes crystalline bulk or interior regions, whereas XPS probes the outermost surface, where partial oxidation, hydroxylation, and adventitious carbon contamination can occur during fabrication and subsequent air exposure.

The TEM images revealed a heterogeneous nanoscale morphology (Figure 4a) comprising compact, nearly spherical particles with dimensions of several tens of nanometers together with larger agglomerated fragments. Clear lattice fringes were observed in the HRTEM images, demonstrating the crystalline character of the particles, while the coexistence of diffraction rings and discrete spots in the SAED patterns indicated a polycrystalline, multidomain structure. EDX analysis yielded a Ru:Ir composition of approximately 81:19 (Figure 4b). The STEM–EDX maps showed substantial spatial co-localization of Ru and Ir within the same particle-rich regions (Figure 4c–f). SEM–EDX analysis over a larger surface area yielded a comparable Ru/Ir composition, confirming that the local STEM–EDX results are representative of the electrode.

The electrochemical properties of the Ru-based composites were evaluated in the presence of glucose. Figure 5a shows the cyclic voltammograms of all fabricated electrodes recorded in a 0.1 M NaOH solution containing 1000 μM glucose. No distinct glucose oxidation peaks were observed in the CV curves for any of the samples. However, the anodic current density within the potential range of 0.4–0.6 V (vs. Ag/AgCl) varied among the materials, with the Ru–Ir composite exhibiting the highest value among both the bimetallic composites and the monometallic Ru and Ir electrodes, supporting a beneficial synergistic effect between Ru and Ir.

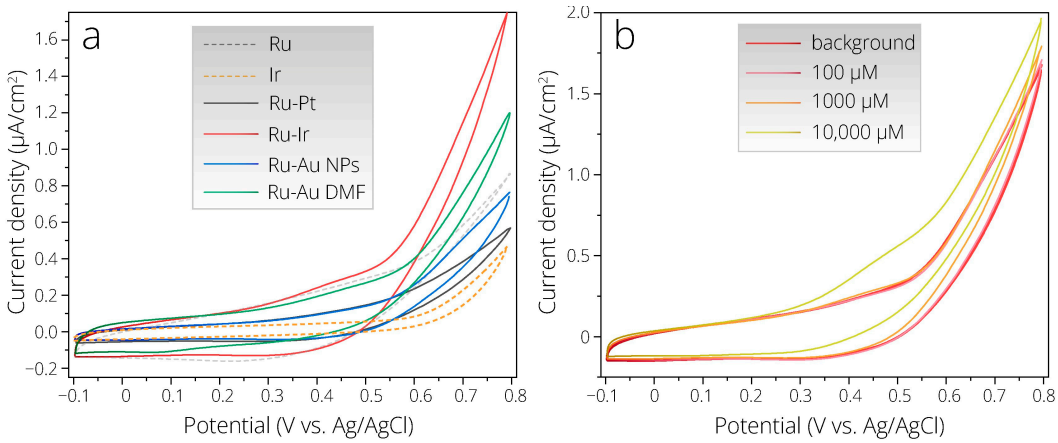

Figure 5. (**a**) CVs of the Ru-based and Ir microstructures recorded in a 0.1 M NaOH solution containing 1000 μM glucose. (**b**) CVs of the Ru–Ir microstructures recorded in a 0.1 M NaOH solution containing glucose at three different concentrations.

The relative electrochemically accessible surface area of the Ru-based bimetallic electrodes was comparatively assessed from their double-layer capacitance, C_{dl}, measured in 0.1 M NaOH within the non-Faradaic potential window from −0.05 to +0.05 V (vs. Ag/AgCl). Among the investigated materials, Ru–Ir exhibited the highest C_{dl} of 0.1249 mF cm^{-2}, suggesting the largest apparent electrochemically accessible interfacial area (Table S2, Figure S1). Although normalization of the glucose-induced current increment to C_{dl} reduced the differences among the electrodes, Ru–Ir retained the highest $\Delta j_{geo}/C_{dl}$ value. Within the limitations of this comparative C_{dl}-based normalization, these results suggest that the enhanced Ru–Ir response cannot be attributed solely to differences in surface accessibility and may also involve a composition-dependent contribution from Ru–Ir interactions. Furthermore, estimation of the apparent heterogeneous electron-transfer rate constant using the Nicholson method with a ferri/ferrocyanide probe gave $k^0_{app} = 4.1 \times 10^{-3}$ cm s^{-1} for Ru–Ir, which is 2.3 times higher than for monometallic Ru (1.8×10^{-3} cm s^{-1}). Additionally, 100 consecutive CV cycles in glucose-containing electrolyte showed no significant degradation of the voltammetric response, confirming stable electrocatalytic performance (Table S2).

To explain this behavior, the mechanism of glucose oxidation must first be considered. According to the mechanism proposed by Pasta et al. [30] for glucose electrooxidation on noble metal surfaces in alkaline media, the process proceeds as follows (Figure 6). First, a glucose molecule is electrochemically adsorbed onto a free metal active site through the anomeric carbon via a dehydrogenation step, forming an adsorbed dehydrogenated intermediate and releasing an adsorbed hydrogen atom. This dehydrogenated intermediate can then be oxidized directly to gluconate in a reaction involving the uptake of a hydroxide ion and the elimination of a proton. Alternatively, the dehydrogenated glucose can be oxidized to δ-gluconolactone. The δ-gluconolactone is subsequently hydrolyzed by a hydroxyl anion from the solution to form gluconate, which then desorbs from the electrode surface [30]. The overall reaction converts glucose to gluconate via a two-electron transfer process.

The absence of a sharp oxidation peak in the cyclic voltammograms, accompanied by a broad current increase in the 0.4–0.5 V range, is characteristic of a surface-controlled electrocatalytic process. As discussed by Pasta et al., the overall current is limited by the kinetics of surface dehydrogenation and the subsequent chemical attack by OH^- ions rather than by the diffusion of glucose from the bulk solution [30]. This limitation results in a drawn-out anodic wave instead of a distinct peak. Similar electrochemical behavior has been reported previously [31].

The higher current density observed for the Ru–Ir composite compared to pure Ru and the other fabricated composites may be related to a possible synergistic effect between the two metals. Iridium has been reported to promote OH^- adsorption at lower overpotentials, which may increase the local concentration of hydroxyl species near the electrode surface. Such an accumulation may facilitate the subsequent nucleophilic attack on the adsorbed dehydrogenated glucose intermediate, thereby potentially accelerating the overall oxidation rate. Additionally, the bimetallic surface may provide a more favorable electronic structure (e.g., through possible tuning of the d-band center) for the initial adsorption and dehydrogenation of glucose, which could contribute to the enhanced catalytic activity [32].

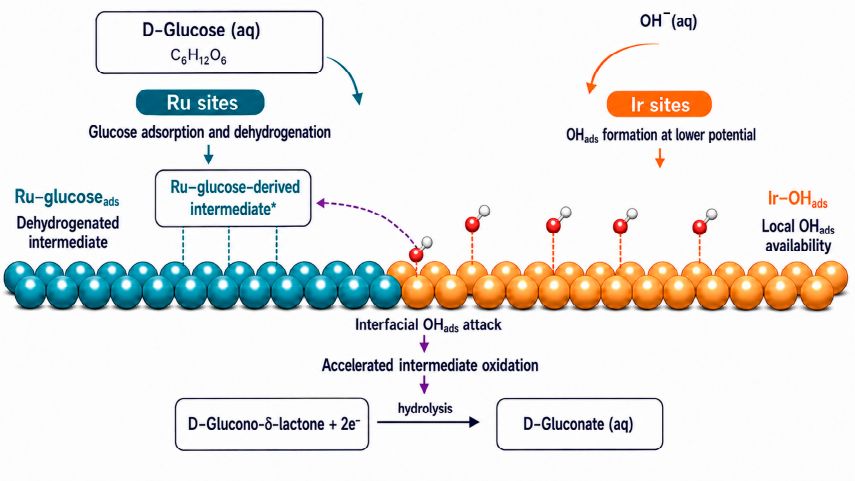

Figure 6. Proposed literature-based mechanism of electrochemical glucose oxidation on the surface of Ru–Ir electrode in alkaline media [32].

Figure 5b shows the cyclic voltammograms of the Ru–Ir electrode recorded in a 0.1 M NaOH solution containing various glucose concentrations. As observed, increasing the glucose concentration led to a progressive current rise in the 0.4–0.6 V range, corresponding to the anodic oxidation of glucose. However, cyclic voltammetry is fundamentally a semi-quantitative technique; its transient nature, caused by the continuous potential sweep, prevents the electrode interface from reaching a true steady state, making it less suitable for precise quantitative analysis [33]. Consequently, for reliable quantitative calibration, chronoamperometry is preferred because it maintains a constant potential and monitors the current over time, allowing the system to approach a steady-state or diffusion-limited current that is directly proportional to the analyte concentration [34]. Upon stepping the potential to a fixed value, the current decay follows a well-defined pattern: an initial sharp drop due to the electrical double-layer charging, followed by a gradual decrease as adsorbed intermediate species form on the electrode surface [35,36]. Once the background current stabilized to a constant baseline, successive aliquots of the analyte were introduced. In the present study, a stabilization period of 900 s was applied before the first glucose addition. The response to 1000 µM glucose increased with potential up to 0.45 V, while further increases produced only a marginal improvement at 0.50 V followed by a slight decrease at 0.55–0.60 V (Figure S2). Therefore, 0.45 V was selected as the lowest potential providing a near-maximal response, maintaining high sensitivity while limiting the potential for nonspecific oxidation.

To further assess the electrochemical control of glucose oxidation, a scan-rate study was performed for the Ru–Ir electrode in 1000 µM glucose. As shown in Figure S3a, the cyclic voltammograms recorded at different scan rates after the addition of 1000 µM glucose showed an increase in the oxidation current with increasing scan rate. The corre-

sponding background cyclic voltammograms recorded at different scan rates are presented in Figure S3b. Figure S3c shows that the blank-subtracted current density at 0.45 V vs. Ag/AgCl ($\Delta j = j_{glucose} - j_{blank}$) increased linearly with scan rate, following $\Delta j = 0.00025v + 0.0053$ ($R^2 = 0.998$). This linear dependence supports a predominantly surface-controlled glucose oxidation process under the investigated conditions.

Figure 7a,b show the chronoamperograms of the Ru–Ir electrode obtained by the successive addition of glucose to the 0.1 M NaOH solution. As observed, the current increases step-wise with each addition of the analyte. Following glucose addition, the Ru–Ir electrode reached 95% of the subsequent steady-state response within approximately 11–13 s. The corresponding calibration curves (Figure 7c), plotted from these steady-state currents including the zero-glucose blank as the 0 µM point, exhibit two distinct linear ranges: 0.5–3000 µM and 3000–12,500 µM. In the low-concentration regime (0.5–3000 µM), the calibration plot follows the linear equation j (µA cm^{-2}) = 22.19 + 0.02685 × C (µM) with a Pearson correlation coefficient (R) of 0.9986, indicating excellent linearity. For the higher concentration range (3000–12,500 µM), the relationship is described by j = 64.6391 + 0.014 × C with a correlation coefficient of 0.9953. The 95% CIs for the fitted slopes were 0.02599–0.02762 and 0.01302–0.01463 µA $µM^{-1}$ cm^{-2}, respectively, and did not overlap, confirming different sensitivities in the two calibration regions. Continuous segmented regression identified a breakpoint at 3155 µM (95% CI: 2857–3530 µM), confirmed a significant slope change ($p < 0.0001$), and strongly favored the segmented over the single-linear model (ΔAICc = 48.50), with no significant lack of fit in either region. The sensitivity, determined by the slope of the calibration curve, is markedly higher in the first range (0.027 µA $µM^{-1}$ cm^{-2}) compared to the second (0.014 µA $µM^{-1}$ cm^{-2}). The limit of detection (LOD) was calculated for the low-concentration range using the 3σ/S method, with σ = 5.20 × 10^{-4} µA cm^{-2} determined from ten independent blank measurements using ten separately fabricated Ru–Ir electrodes. The resulting LOD was 58.1 nM, with a corresponding LOQ (10σ/S) of 0.194 µM. Furthermore, a standard-addition calibration was performed using five aliquots of the undiluted test sample nominally containing 1000 µM glucose, spiked with 0, 100, 250, 500, and 750 µM glucose. Recoveries of 97.9–102.1% confirmed the high analytical predictive performance of the Ru–Ir sensor (Table S3).

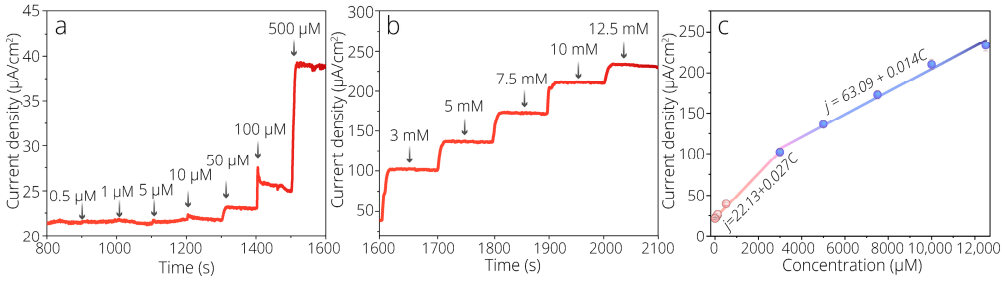

Figure 7. Amperometric responses of the Ru–Ir electrode to the successive addition of glucose in a 0.1 M NaOH solution at 0.45 V (vs. Ag/AgCl) within the (**a**) low (0.5–3000 µM) and (**b**) high (3000–12,500 µM) concentration ranges. (**c**) Corresponding calibration plots of current density versus glucose concentration.

The presence of two linear regions is frequently observed for nanostructured electrocatalysts and may be associated with the hierarchical surface morphology of the Ru–Ir composite and the presence of electroactive sites with different properties. At low glucose concentrations, the most accessible and highly active sites may contribute preferentially to glucose oxidation, resulting in higher sensitivity. At higher concentrations, partial saturation of these sites and an increasing contribution from less active or diffusion-limited sites could account for the lower apparent sensitivity. Similar dual-range calibration behaviors

have been reported previously for other hierarchically structured metal electrodes [24]. This interpretation remains a plausible hypothesis and requires further mechanistic investigation. The high Pearson coefficients indicate strong linear association within the two fitted concentration ranges.

In addition, the exceptional electrochemical performance of the developed non-enzymatic glucose sensor (LOD = 58.1 nM) is presumably governed by a synergetic effect between iridium (Ir) and ruthenium (Ru), operating via a bifunctional catalytic mechanism. Within this bimetallic architecture, the two metals are proposed to contribute through distinct roles that may help overcome the limitations of single-metal systems. Ruthenium serves as the primary catalytic matrix responsible for the initial activation of the analyte. Due to its optimized d-band electronic structure, the Ru sites facilitate the efficient chemisorption of glucose molecules and accelerate the rate-determining step, which involves the cleavage of the anomeric C–H bond. Concurrently, iridium acts as a powerful promoter to prevent surface passivation, a common bottleneck caused by the accumulation of strongly adsorbed, poisoning intermediates (such as CO-like species) on ruthenium. It exhibits a unique ability to induce the dissociative chemisorption of water at lower potentials, generating an abundance of surface hydroxyl groups (-OH_{ads}). These highly reactive hydroxyl species oxidatively convert the poisoning intermediates into soluble carbonates, thereby continuously clearing and regenerating the active Ru sites. Furthermore, the electronic interaction (ligand effect) arising from Ir–Ru coupling may modulate the adsorption energies and facilitate product desorption. Coupled with the intrinsic chemical and electrochemical robustness of iridium, this bifunctional synergy simultaneously achieves ultra-high sensitivity and remarkable operational stability [37–39].

The selectivity, reproducibility, and long-term stability of the Ru–Ir sensor were evaluated using chronoamperometry. Selectivity was assessed toward glucose in the presence of common potentially interfering species, including dopamine (DA), ascorbic acid (AA), uric acid (UA), acetaminophen (AP), hydrogen peroxide (H_2O_2), and fructose (Fru), each at 30 μM, together with chloride ions (Cl^-, 10 mM). The 30 μM concentration was selected as a conservative screening challenge for an approximately 100-fold diluted biological sample, in which the expected concentrations of UA, AA, fasting fructose, therapeutic AP, and dopamine are approximately 1.8–5.1, 0.5–0.8, 0.06, <2, and $\ll$1 μM, respectively [40–44], whereas Cl^- was included at 10 mM to assess possible chloride-induced inhibition of the Ru–Ir surface. In a typical experiment, glucose (50 μM) was initially introduced into the 0.1 M NaOH solution, followed by the successive addition of interferents (each at 30 μM), and finally, a second aliquot of glucose (50 μM) (Figure 8a). The resulting chronoamperogram demonstrates that the current responses generated by the interfering species are negligible compared to the signal evoked by glucose. These findings indicate a preferential response to glucose in the presence of the investigated potentially interfering species under the tested conditions. To support the selectivity assessment, analytical performance in a plasma-like matrix was evaluated using glucose-free Artificial Plasma Fluid spiked with 2.50, 5.00, and 10.00 mM glucose, corresponding to hypoglycemic, normoglycemic, and hyperglycemic levels, respectively, and analyzed after ten-fold dilution to a final NaOH concentration of 0.100 M. The resulting concentrations of 250, 500, and 1000 μM were quantified using the low-concentration calibration curve, yielding recoveries of 97.9–101.2%, relative biases of −2.1% to +1.2%, and RSD values of 1.73–2.80% (Table S4).

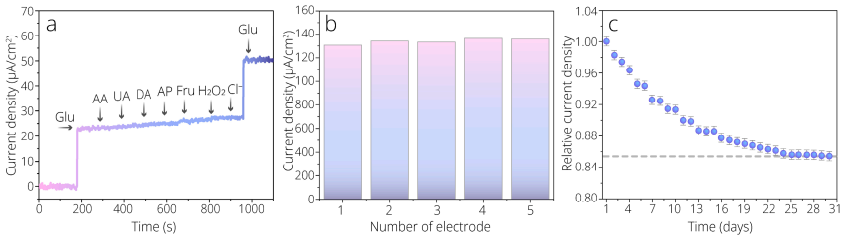

Figure 8. (**a**) Chronoamperometric response of the Ru–Ir electrode to the sequential addition of glucose (50 μM), various interferents, and a subsequent second aliquot of glucose (50 μM) in a 0.1 M NaOH solution at 0.45 V. (**b**) Amperometric responses of five independently fabricated Ru–Ir electrodes toward 5000 μM glucose at 0.45 V. (**c**) Long-term stability of the Ru–Ir electrode toward 5000 μM glucose over 30 days.

The reproducibility of the Ru–Ir sensor was evaluated using five independently fabricated electrodes. Figure 8b shows the amperometric responses recorded in the presence of 5000 μM glucose at a constant potential of 0.45 V. The relative standard deviation (RSD) calculated from these measurements was 2.33%, indicating the high reproducibility of the proposed fabrication protocol. The long-term stability was investigated by measuring the amperometric response of a Ru–Ir electrode to a 5000 μM glucose solution daily over a 30-day period (n = 3, RSD = 2.4%). Between measurements, the electrodes were stored dry under ambient laboratory conditions at 23 ± 2 °C and approximately 30 ± 5% relative humidity, without active temperature or humidity control. As displayed in Figure 8c, the sensor retained more than 85% of its initial current response after one month of operation, demonstrating the excellent long-term stability of the developed material. A separate intra-electrode repeatability experiment was performed using the same Ru–Ir electrode over ten successive measurement cycles at 5000 μM glucose under otherwise identical conditions. Each cycle used freshly prepared 0.1 M NaOH, followed by rinsing with deionized water without mechanical polishing or electrochemical regeneration. The ten responses yielded an intra-electrode RSD of 2.56%, while the tenth response retained 98.3% of the first. Together with the stable response observed over 100 CV cycles, these results indicate good short-term repeatability and no evidence of progressive electrode fouling under the investigated conditions.

To critically evaluate the analytical performance of the developed Ru–Ir sensor, its key sensing parameters were compared with previously reported non-enzymatic glucose sensors based on noble metals and their bimetallic counterparts (Table 2). As summarized in the table, the fabricated Ru–Ir microstructures demonstrate a highly competitive limit of detection (58.1 nM) and an exceptionally wide dual-range linearity (0.5 to 3000 μM and 3000 to 12,500 μM). These values compare favorably with those reported for published non-enzymatic glucose-sensing platforms. While several literature-reported materials (Table 2) achieve comparable sensitivities, their fabrication protocols frequently rely on multi-step hydrothermal processes, electrodeposition, or complex chemical reduction methods that require sacrificial templates or lithographic masks. Furthermore, conventional electrode modification often necessitates the use of non-conductive polymer binders (e.g., Nafion or PTFE), which can block active catalytic centers and hinder mass transport. In contrast, the laser-induced chemical liquid-phase deposition technique proposed in this work offers a straightforward, mask-free, and binder-free route to generate highly conductive, porous bimetallic networks directly on the substrate. Consequently, the outstanding sensitivity, combined with the technological simplicity of the LCLD approach (continuous-wave laser operation, conventional focusing optics and motorized positioning, and processing under ambient conditions), highlights the developed Ru–Ir composite as a superior alternative for advanced non-enzymatic glucose detection platforms.

Table 2. Comparison of the analytical performance of the developed Ru–Ir sensor with various literature-reported non-enzymatic glucose detection platforms.

Electrode Material	Fabrication Method	Supporting Electrolyte/pH	Potential (V vs. Ag/AgCl)	Linear Range (μM)	Sensitivity (μA μM^{-1} cm^{-2})	LOD, μM	Response Time (s)	Real-Sample Validation	Stability	Ref.
Ru–Ir microstructures	Two-stage LCLD	0.1 M NaOH	0.45	0.5–3000/3000–12,500	0.02685/0.014	0.0581 (58.1 nM)	11–13	Artificial Plasma Fluid; recovery 97.9–101.2%	>85% after 30 days	This work
Cu@Ni Core–Shell/Carbon Nanocoils	CVD growth on nickel foam (NF) + solvothermal synthesis	0.1 M NaOH	0.55	0.1–1300	6.905	0.03	0.1	Human serum; recovery 96.6–102.1%	81% after 30 days	[45]
Au NF carbon cloth	Chemical reduction method	PBS, pH 7.4	0.35	8–4000	63.9	5.18	2.3	Human sweat; demonstrated monitoring before/after meal	Long-term stability data not provided; only response-recovery characteristics are reported	[46]
Pd@Pt CNCC	Epitaxial growth method	0.1 M PBS, pH 7.4	0.45	2400–10,600	0.01106	0.15	Not explicitly stated	Serum; recovery 98.80–99.85%; RSD ≤ 1.06%	No numerical retention percentage or number of cycles provided	[47]
Ru@NiCo-MOF/	Chemical deposition	0.1 M NaOH	0.65	10–670/670–5070	1.07077/0.48762	0.446	2	Human saliva	89.6% after 16 days	[48]
AuRu-modified CNT-PtNP	Screen-printing + electrodeposition	0.01 M PBS, pH 7.4	−0.10	1000–10,000	0.02347	68.0	240	Human serum and porcine whole blood	>87% of initial sensitivity after 3 weeks at 37 °C; RSD = 3.87% for 5 sensors	[49]
$Cu_{53}@Ni_{47}$ CSNPs/rGO/GCE	Solvothermal (one-pot)	0.1 M NaOH	+0.575 V (vs. SCE)	1–4100	0.780	0.5	3	Simulative serum (1 mM glucose + 0.08 mM AA + 0.04 mM UA); recovery 95.2–104.3% (n = 3)	93% after 72 h (4 °C); 89% with rGO	[50]
Au@Ni/C (core–shell)	Oleylamine reduction + loading on carbon	0.1 M NaOH	0.10 V vs. SCE	500–10,000	0.02317	15.7	3	Fermentation broth (qualitative anti-interference to fructose, lactose, sucrose, AA); no numerical recovery provided	>90% after 7 days (stored in air)	[51]
Cu@C nanocubes/Nafion/GCE	Annealing of Cu_2O@PVP at 600 °C	0.4 M NaOH	0.6 V vs. SCE	40–40,000	2.565	21.35	5	Human serum (diluted 100×); recovery 98.78–101.04% (n = 3), RSD 0.71–4.8%	95% after 2 months	[52]

4. Conclusions

In this work, a series of ruthenium-based bimetallic microstructures (Ru–Ir, Ru–Pt, Ru–Au DMF, and Ru-Au NPs) were successfully fabricated on glass substrates using a two-stage laser-induced chemical liquid-phase deposition technique. Among the prepared composites, the Ru–Ir electrode exhibited the highest electrocatalytic activity toward glucose oxidation in an alkaline medium. The superior performance of the Ru–Ir sensor is attributed to its highly developed hierarchical surface morphology, which provides abundant electroactive sites, and a synergetic effect between ruthenium and iridium that enhances the adsorption of hydroxyl species and accelerates the surface-controlled dehydrogenation of glucose. Cyclic voltammetry revealed a concentration-dependent current increase within the 0.4–0.6 V range without a distinct oxidation peak. Under chronoamperometric conditions at an operating potential of 0.45 V, the Ru–Ir electrode displayed two linear calibration ranges (0.5–3000 μM and 3000–12,500 μM) with sensitivities of 0.027 and 0.014 μA μM^{-1} cm^{-2}, respectively. The limit of detection was determined to be 58.1 nM. Selectivity tests against common interferents (ascorbic acid, uric acid, acetaminophen, and hydrogen peroxide) demonstrated negligible cross-sensitivity, confirming the outstanding selectivity of the sensor. Furthermore, the electrode showed excellent reproducibility (RSD = 2.33% for five independently fabricated sensors) and remarkable long-term stability, retaining more than 85% of its initial response after 30 days of daily measurements. The proposed LCLD approach offers a simple and mask-free route for the fabrication of binder-free bimetallic electrodes with a tunable surface architecture. Consequently, the favorable analytical performance of the developed Ru–Ir material, including its low detection and quantification limits and broad calibration range, supports its potential use for ex situ glucose analysis following controlled alkaline dilution.

Supplementary Materials: The following supporting information can be downloaded at: https://www.mdpi.com/article/10.3390/analytica7030067/s1. Table S1: Calibration data obtained using three independently fabricated Ru–Ir electrodes. Mean values are reported without background correction; Table S2: Double-layer capacitance (C_{dl}) and glucose response per unit capacitance for the Ru-based bimetallic electrodes; Figure S1: Dependence of the capacitive current density on the scan rate for Ru–Pt, Ru–Au NPs, Ru–Au DMF, and Ru–Ir electrodes. Solid lines represent linear fits used to determine the double-layer capacitance (C_{dl}) from the slopes. Data are presented as mean ± SD; Figure S2: Effect of the applied potential on the amperometric response to 1000 μM glucose. The response was calculated as the blank-corrected current density ($\Delta j = j_{glucose} - j_{blank}$). Data are presented as mean ± SD (n = 3); Figure S3: (a) Cyclic voltammograms recorded at different scan rates after addition of 1000 μM glucose, (b) background cyclic voltammograms recorded at different scan rates, and (c) dependence of the current density measured at 0.45 V vs. Ag/AgCl on the scan rate. (d) Logarithmic plot of Δj measured at 0.45 V vs. Ag/AgCl as a function of scan rate, yielding a power-law exponent b = 0.72. (e) Dunn-type analysis of the current response according to $\Delta j = k_{1v} + k_{2v}{}^{1/2}$, illustrating the contributions of surface-associated and diffusion-dependent processes; Table S3: Recovery of glucose by the standard addition method using the Ru–Ir electrode; Table S4: Recovery of glucose from spiked Artificial Plasma Fluid using the Ru–Ir sensor (n = 3).

Author Contributions: Conceptualization: A.V.V., A.P.Z., M.S.P. and E.M.K.; Data Curation: A.V.V., A.P.Z., M.K. and S.G.; Formal Analysis: A.V.V., A.P.Z., A.S.L., D.M.N. and S.G.; Funding Acquisition: M.S.P. and A.V.V.; Investigation: A.V.V., A.P.Z., A.S.L., M.K. and D.M.N.; Methodology: M.S.P. and E.M.K.; Project Administration: M.S.P.; Resources: M.S.P. and A.V.V.; Supervision: M.S.P. and E.M.K.; Validation: A.V.V., E.M.K., A.S.L. and M.K.; Visualization: E.M.K. and A.S.L.; Writing—Original Draft: A.V.V., M.S.P. and E.M.K.; Writing—Review and Editing: M.S.P., E.M.K., A.V.V., A.P.Z., A.S.L., M.K., S.G., D.M.N. and M.N.R. All authors have read and agreed to the published version of the manuscript.

Funding: This research was financially supported by the Ministry of Science and Higher Education of the Russian Federation (Project FSRM-2026-0027). SEM studies and determination of phase composition were supported by St. Petersburg State University, project code 125021702335-5.

Data Availability Statement: Data available on request.

Acknowledgments: The authors would also like to thank the SPBU Research Park, especially the Nanotechnology Interdisciplinary Centre, the Centre for X-ray Diffraction Studies, and the Centre for Optical and Laser Materials Research. During the preparation of this manuscript, GPT-5.6 (OpenAI) was used for language editing and to assist with the initial sketching of Figure 6. All AI-assisted content was subsequently reviewed, verified, and approved by the authors, who take full responsibility for the final content of the manuscript.

Conflicts of Interest: The authors declare no conflicts of interest.

Abbreviations

The following abbreviations are used in this manuscript:

LCLD	Laser-induced chemical liquid-phase deposition
SEM	Scanning electron microscopy
EDX	Energy-dispersive X-ray spectroscopy
XRD	X-ray diffraction
CV	Cyclic voltammetry
DMF	N,N-dimethylformamide
LOD	Limit of detection
RSD	Relative standard deviation

References

1. Dong, Q.; Ryu, H.; Lei, Y. Metal oxide based non-enzymatic electrochemical sensors for glucose detection. *Electrochim. Acta* **2021**, *370*, 137744. [CrossRef]
2. Karimi-Maleh, H.; Cellat, K.; Arıkan, K.; Savk, A.; Karimi, F.; Şen, F. Palladium–Nickel nanoparticles decorated on functionalized MWCNT for high precision non-enzymatic glucose sensing. *Mater. Chem. Phys.* **2020**, *250*, 123042. [CrossRef]
3. Davaji, B.; Lee, C.H. A paper-based calorimetric microfluidics platform for bio-chemical sensing. *Biosens. Bioelectron.* **2014**, *59*, 120–126. [CrossRef] [PubMed]
4. Maruthupandy, M.; Rajivgandhi, G.; Muneeswaran, T.; Vennila, T.; Quero, F.; Song, J.M. Chitosan/silver nanocomposites for colorimetric detection of glucose molecules. *Int. J. Biol. Macromol.* **2019**, *121*, 822–828. [CrossRef] [PubMed]
5. Tsao, C.W.; Yang, Z.J. High sensitivity and high detection specificity of gold-nanoparticle-grafted nanostructured silicon mass spectrometry for glucose analysis. *ACS Appl. Mater. Interfaces* **2015**, *7*, 22630–22637. [CrossRef] [PubMed]
6. Van Tam, T.; Hur, S.H.; Chung, J.S.; Choi, W.M. Novel paper- and fiber optic-based fluorescent sensor for glucose detection using aniline-functionalized graphene quantum dots. *Sens. Actuators B Chem.* **2021**, *329*, 129250. [CrossRef]
7. Cho, M.J.; Park, S.Y. Carbon-dot-based ratiometric fluorescence glucose biosensor. *Sens. Actuators B Chem.* **2019**, *282*, 719–729. [CrossRef]
8. Li, D.; Zhang, S.; Feng, X.; Yang, H.; Nie, F.; Zhang, W. A novel peroxidase mimetic Co-MOF enhanced luminol chemiluminescence and its application in glucose sensing. *Sens. Actuators B Chem.* **2019**, *296*, 126631. [CrossRef]
9. Qi, Y.; Sun, Y.; Song, D.; Wang, Y.; Xiu, F. PVC dechlorination residues as new peroxidase-mimicking nanozyme and chemiluminescence sensing probe with high activity for glucose and ascorbic acid detection. *Talanta* **2023**, *253*, 124039. [CrossRef]
10. Bari, S.M.I.; Reis, L.G.; Nestorova, G.G. Numerical optimization of key design parameters of a thermoelectric microfluidic sensor for ultrasensitive detection of biochemical analytes. *J. Therm. Sci. Eng. Appl.* **2021**, *13*, 021024. [CrossRef]
11. Thatikayala, D.; Ponnamma, D.; Sadasivuni, K.K.; Cabibihan, J.J.; Al-Ali, A.K.; Malik, R.A.; Min, B. Progress of advanced nanomaterials in the non-enzymatic electrochemical sensing of glucose and H_2O_2. *Biosensors* **2020**, *10*, 151. [CrossRef] [PubMed]
12. Sehit, E.; Altintas, Z. Significance of nanomaterials in electrochemical glucose sensors: An updated review (2016–2020). *Biosens. Bioelectron.* **2020**, *159*, 112165. [CrossRef] [PubMed]
13. Wang, J. Electrochemical Glucose Biosensors. *Chem. Rev.* **2008**, *108*, 814–825. [CrossRef] [PubMed]
14. Toghill, K.E.; Compton, R.G. Electrochemical non-enzymatic glucose sensors: A perspective and an evaluation. *Int. J. Electrochem. Sci.* **2010**, *5*, 1246–1301. [CrossRef]

15. Hwang, D.W.; Lee, S.; Seo, M.; Chung, T.D. Recent advances in electrochemical non-enzymatic glucose sensors—A review. *Anal. Chim. Acta* **2018**, *1033*, 1–34. [CrossRef] [PubMed]
16. Wierzbicka, E.; Sulka, G.D. Nanoporous spongelike Au–Ag films for electrochemical epinephrine sensing. *J. Electroanal. Chem.* **2016**, *762*, 43–50. [CrossRef]
17. Jeon, J.H.; Lim, H.-R.; Park, J.Y.; Choa, Y.-H. Iridium oxide-based non-enzymatic glucose sensor: Superior electro-catalytic performance in biological environmental media. *Environ. Res.* **2024**, *252*, 118772. [CrossRef] [PubMed]
18. Wang, Z.; Bi, X.; Tang, L.; Sun, H.; Cao, Z.; Jiang, C. In-situ generation of Co-Fe bimetallic electrocatalysts on lignosulfonate-derived graphene by direct laser writing for wearable glucose biosensors. *Sens. Actuators B Chem.* **2025**, *432*, 137506. [CrossRef]
19. Song, Q.; Xiao, Z.; Gao, H.; Chen, X.; Cheng, L.; King, J.-L.; Zhu, M.; Mao, Y. Sensor fabrication assisted by initiated chemical vapor deposition. *ACS Macro Lett.* **2025**, *14*, 1631–1639. [CrossRef] [PubMed]
20. Zhou, Y.; Yang, S.; Qian, Q.-Y.; Akiiga, N.S.; Li, J.; Wang, Y.; Zheng, G.; Xia, X.-H.; Abd El-Moneim, A.A. Enzyme-free glucose detection in sweat using 2D inkjet-printed cobalt sulfide anchored on graphene in a paper-based microfluidic device. *J. Colloid Interface Sci.* **2025**, *688*, 144–154. [CrossRef] [PubMed]
21. De Bortoli, L.S.; Vanoni, C.R.; Jost, C.L.; Mezalira, D.Z.; Fredel, M.C. Stable and ligand-free gold nanoparticles produced by laser ablation as efficient electrocatalysts for electrochemical sensing of dopamine. *J. Electroanal. Chem.* **2023**, *947*, 117744. [CrossRef]
22. Sasahara, T.; Tamaki, T.; Nakayama, K.; Uchiyama, Y.; Mizoshiri, M. Copper-based electrodes fabricated by GHz-burst femtosecond laser sintering of copper powders for non-enzymatic D-glucose detection. *Appl. Phys. A* **2026**, *132*, 495. [CrossRef]
23. Panov, M.S.; Nikolaev, D.M.; Shtyrov, A.A.; Mereshchenko, A.S.; Vasin, A.V.; Ryazantsev, M.N. Ruthenium-based microstructures modified by gold particles as composite electrode material for non-enzymatic epinephrine detection. *Microchem. J.* **2024**, *206*, 111507. [CrossRef]
24. Panov, M.S.; Zakharov, A.P.; Khairullina, E.M.; Tumkin, I.I.; Mereshchenko, A.S.; Nikolaev, D.M.; Vasin, A.V.; Ryazantsev, M.N. Au–Ru composite for enzyme-free epinephrine sensing. *Chemosensors* **2022**, *10*, 513. [CrossRef]
25. Kim, D.; Choi, C. Laser-induced metal reduction from liquid electrolyte precursor. *J. Nanosci. Nanotechnol.* **2013**, *13*, 7581–7585. [CrossRef] [PubMed]
26. Kordás, K.; Békési, J.; Vajtai, R.; Nánai, L.; Leppävuori, S.; Uusimäki, A.; Bali, K.; George, T.F.; Galbács, G.; Ignácz, F.; et al. Laser-assisted metal deposition from liquid-phase precursors on polymers. *Appl. Surf. Sci.* **2001**, *172*, 178–189. [CrossRef]
27. Dykman, L.A.; Khlebtsov, N.G. Methods for chemical synthesis of colloidal gold. *Russ. Chem. Rev.* **2019**, *88*, 229–247. [CrossRef]
28. Bag, A.; Ghorai, P.K. Computational investigation of the ligand field effect to improve the photoacoustic properties of organometallic carbonyl clusters. *RSC Adv.* **2015**, *5*, 31575–31583. [CrossRef]
29. Panov, M.S.; Khairullina, E.M.; Vshivtcev, F.S.; Ryazantsev, M.N.; Tumkin, I.I. Laser-induced synthesis of composite materials based on iridium, gold and platinum for non-enzymatic glucose sensing. *Materials* **2020**, *13*, 3359. [CrossRef] [PubMed]
30. Pasta, M.; La Mantia, F.; Cui, Y. Mechanism of glucose electrochemical oxidation on gold surface. *Electrochim. Acta* **2010**, *55*, 5561–5568. [CrossRef]
31. Neha, N.; Rafaïdeen, T.; Faverge, T.; Maillard, F.; Chatenet, M.; Coutanceau, C. Revisited mechanisms for glucose electrooxidation at platinum and gold nanoparticles. *Electrocatalysis* **2023**, *14*, 121–130. [CrossRef]
32. Borja, P.; Vicent, C.; Baya, M.; García, H.; Mata, J.A. Iridium complexes catalysed the selective dehydrogenation of glucose to gluconic acid in water. *Green Chem.* **2018**, *20*, 4094–4101. [CrossRef]
33. Cancelliere, R.; Molinara, M.; Licheri, A.; Maffucci, A.; Micheli, L. Artificial intelligence-assisted electrochemical sensors for qualitative and semi-quantitative multiplexed analyses. *Digit. Discov.* **2025**, *4*, 338–342. [CrossRef]
34. Phasuksom, K.; Sirivat, A. Chronoampermetric detection of enzymatic glucose sensor based on doped polyindole/MWCNT composites modified onto screen-printed carbon electrode as portable sensing device for diabetes. *RSC Adv.* **2022**, *12*, 28505–28518. [CrossRef] [PubMed]
35. Conceição, V.S.; Saraiva, D.P.M.; Denuault, G.; Bertotti, M. Calibration-Free Analysis with Chronoamperometry at Microelectrodes. *Anal. Chem.* **2024**, *96*, 14766–14774. [CrossRef] [PubMed]
36. Scandurra, A.; Iacono, V.; Boscarino, S.; Scalese, S.; Grimaldi, M.G.; Ruffino, F. Model of Chronoamperometric Response towards Glucose Sensing by Arrays of Gold Nanostructures Obtained by Laser, Thermal and Wet Processes. *Nanomaterials* **2023**, *13*, 1163. [CrossRef] [PubMed]
37. Liu, Y.; Tao, X.; Huang, C.; Zhao, K.; Deng, B.; Peng, F. Regulating Adsorption Selectivity by Charge-Polarized $Au^{\delta-}$–$Cu^{\delta+}$ Site for Stable Glucose Electrooxidation. *Nat. Commun.* **2026**, *17*, 4372. [CrossRef] [PubMed]
38. Faverge, T.; Gilles, B.; Bonnefont, A.; Maillard, F.; Coutanceau, C.; Chatenet, M. In Situ Investigation of d-Glucose Oxidation into Value-Added Products on Au, Pt, and Pd under Alkaline Conditions: A Comparative Study. *ACS Catal.* **2023**, *13*, 2657–2669. [CrossRef]
39. Er, O.F.; Kivrak, H. Highly Active Carbon Nanotube Supported Iridium, Copper, Ruthenium Catalysts for Glucose Electrooxidation. *Energy Storage* **2021**, *3*, e271. [CrossRef]

40. Yang, J.; Wu, J.; Liu, Q.; Nan, J.; Zhao, H.; Yuan, H. Establishment of reference intervals for serum uric acid among adults in China. *iLABMED* **2025**, *3*, 209–220. [CrossRef]
41. Lykkesfeldt, J.; Carr, A.C.; Tveden-Nyborg, P. The pharmacology of vitamin C. *Pharmacol. Rev.* **2025**, *77*, 100043. [CrossRef] [PubMed]
42. Buziau, A.M.; Scheijen, J.L.; Stehouwer, C.D.; Simons, N.; Brouwers, M.C.; Schalkwijk, C.G. Development and validation of a UPLC-MS/MS method to quantify fructose in serum and urine. *J. Chromatogr. B* **2020**, *1155*, 122299. [CrossRef] [PubMed]
43. Ayoub, S.S. Paracetamol (acetaminophen): A familiar drug with an unexplained mechanism of action. *Temperature* **2021**, *8*, 351–371. [CrossRef] [PubMed]
44. Gwon, Y.; Kim, J.-H.; Lee, S.-W. Quantification of plasma dopamine in depressed patients using silver-enriched silicon nanowires as SERS-active substrates. *ACS Sens.* **2024**, *9*, 870–882. [CrossRef] [PubMed]
45. Farid, A.; Khan, A.S.; Javid, M.; Usman, M.; Khan, I.A.; Ahmad, A.U.; Fan, Z.; Khan, A.A.; Pan, L. Construction of a binder-free non-enzymatic glucose sensor based on Cu@Ni core–shell nanoparticles anchored on 3D chiral carbon nanocoils-nickel foam hierarchical scaffold. *J. Colloid Interface Sci.* **2022**, *624*, 320–337. [CrossRef] [PubMed]
46. Zhao, Z.; Wang, T.; Li, K.; Long, D.; Zhao, J.; Zhu, F.; Gong, W. A flexible nonenzymatic sweat glucose sensor based on Au nanoflowers coated carbon cloth. *Sens. Actuators B Chem.* **2023**, *388*, 133798. [CrossRef]
47. Wang, S.S.; Qiu, W.J.; Wang, T.P.; Lee, C.L. Tuning structures of Pt shells on Pd nanocubes as neutral glucose oxidation catalysts and sensors. *Appl. Surf. Sci.* **2022**, *605*, 154670. [CrossRef]
48. Liao, L.; Xu, F.; Sun, L.; Luo, Y.; Guan, Y.; Xie, Y.; Zeng, J. Fabrication of a novel non-enzymatic glucose sensor based on ruthenium supported by a combination of PBA nanocubes and MOF nanosheets. *Microchem. J.* **2024**, *207*, 111791. [CrossRef]
49. Nguyen, T.N.H.; Jin, X.; Nolan, J.K.; Xu, J.; Le, K.V.H.; Lam, S.; Wang, Y.; Alam, M.A.; Lee, H. Printable nonenzymatic glucose biosensors using carbon nanotube-PtNP nanocomposites modified with AuRu for improved selectivity. *ACS Biomater. Sci. Eng.* **2020**, *6*, 5315–5325. [CrossRef] [PubMed]
50. Wu, K.L.; Cai, Y.M.; Jiang, B.B.; Cheong, W.C.; Wei, X.W.; Wang, W.; Yu, N. Cu@Ni core–shell nanoparticles/reduced graphene oxide nanocomposites for nonenzymatic glucose sensor. *RSC Adv.* **2017**, *7*, 21128–21135. [CrossRef]
51. Gao, X.; Du, X.; Liu, D.; Gao, H.; Wang, P.; Yang, J. Core-shell gold-nickel nanostructures as highly selective and stable nonenzymatic glucose sensor for fermentation process. *Sci. Rep.* **2020**, *10*, 1365. [CrossRef] [PubMed]
52. Ye, J.; Deng, D.; Wang, Y.; Luo, L.; Qian, K.; Cao, S.; Feng, X. Well-aligned Cu@C nanocubes for highly efficient nonenzymatic glucose detection in human serum. *Sens. Actuators B.* **2020**, *305*, 127473. [CrossRef]